Research Square

Preprints are preliminary reports that have not undergone peer review.
They should not be considered conclusive, used to inform clinical practice,
or referenced by the media as validated information.

Hydraulic Performance Variation and Anti-clogging Regulatory Mechanisms of an Auto-flushing Emitter for Drip Irrigation under Sediment-Laden Water Conditions

Qiameng Du
Tarim University
Yan Mo
moyansdi@163.com
China Institute of Water Resources and Hydropower Research
Baolin Yao
Tarim University
Hao Gao
China Institute of Water Resources and Hydropower Research
Zongze Yang
China Institute of Water Resources and Hydropower Research
Yanqun Zhang
China Institute of Water Resources and Hydropower Research
Hao Li
China Institute of Water Resources and Hydropower Research
Sanmin Sun
Tarim University

Research Article

Keywords: auto-flushing emitter, sediment-laden water, elastomer, activation pressure threshold, flow cross-sectional area, incipient motion velocity

Posted Date: November 19th, 2026

DOI: https://doi.org/10.21203/rs.3.rs-11602371/v1

License: This work is licensed under a Creative Commons Attribution 4.0 International License.
Read Full License

Additional Declarations: No competing interests reported.

Hydraulic Performance Variation and Anti-clogging Regulatory Mechanisms of an Auto-flushing Emitter for Drip Irrigation under Sediment-Laden Water Conditions

Qiameng Du[1,2], Yan Mo[1*], Baolin Yao[2], Hao Gao[1], Zongze Yang[1,3], Yanqun Zhang[1], Hao Li[1], Sanmin Sun[2]

1. State Key Laboratory of Basin Water Cycle and Water Security, China Institute of Water Resources and Hydropower Research, Beijing 100048, China

2. College of Water Conservancy and Architectural Engineering, Tarim University, Alaer 843300, China

3. Shanxi Agricultural Planning and Design Research Institute Co, Ltd, Taiyuan, Shanxi 030002, China

* Corresponding author at: State Key Laboratory of Basin Water Cycle and Water Security, China Institute of Water Resources and Hydropower Research, Beijing 100048, China
E-mail address: moyansdi@163.com (Y. Mo).

Abstract

Emitter clogging severely limits drip irrigation using sediment-laden water. This study developed a novel auto-flushing emitter (AFE) with deformable elastomers, which switches between normal irrigation and auto-flushing modes via pressure-induced deformation that enlarges the flow cross-section. Three emitter cores (EMI1, EMI2, EMI3) paired with three elastomers (silicone, SI; polyurethane, PU; non-deformable PTFE as the control, CK) were tested under clean water and sediment-laden water (2 g/L, d50 = 34.84 μm). Under clean water, the AFE flow rate (q_{CW}) increased stepwise with inlet pressure (H_0), with an activation pressure threshold (H_j) of 0.07–0.10 MPa. When $H_0 > H_j$, q_{CW} of the SI-fitted AFEs was 9.18–

50.58% higher than that of the CKs. Under sediment-laden water, the average relative discharge (*Dra*) of all nine emitters declined with operating time, but this decline weakened at higher H_0 and with softer elastomers. At 360 min, *Dra* of the SI-fitted AFEs exceeded PU-fitted and CKs by 14.2% and 30.2%, respectively. For AFEs, rising H_0 enlarged the flow cross-sectional area (S) and reduced mean flow velocity (v), whereas v increased in the CKs. Compared with PU-fitted AFEs and CKs, S of SI-fitted AFEs increased by 3.71–6.79% and 66.91–249.13%, respectively, and v (0.24–0.41 m/s) of the three SI-fitted AFEs overlapped the sediment incipient-motion velocity (0.07–0.70 m/s). Correlation and regression analyses show that expanded S under auto-flushing is the primary driver of improved anti-clogging performance. These findings provide technical support for AFE development and sediment-laden water drip-irrigation application.

Keywords: auto-flushing emitter; sediment-laden water; elastomer; activation pressure threshold; flow cross-sectional area; incipient motion velocity

Nomenclature

		PU	Polyurethane
		q_{CW}	Clean water emitter flow rate (L/h)
A	Tooth angle (°)	q_{SW}	The sediment-laden flow rate (L/h)
AFE	Auto-flushing emitter	S	Flow cross-sectional area (mm^2)
B	Tooth spacing (mm)	S_1	Original flow-channel cross-sectional area (mm^2)
CK	Non-deformable PTFE-fitted control emitters	S_2	Additional cross-sectional area when SI is fully deformed (mm^2)

CW	Clean water tests	SI	Silicone
D	Flow channel depth (mm)	SS_{PU}	Shore-A hardness of PU elastomer (HA)
Dra	The average relative discharge (%)	SS_{SI}	Shore-A hardness of SI elastomer (HA)
E	Tooth height (mm)	SW	Sediment-laden water tests
EMI	Core of AFE	T	Operating times (min)
h	The hydraulic radius (mm)	U_c	The incipient motion velocity of sediment particles (m/s)
H_0	Inlet water pressure (MPa)	v	The cross-sectional average flow velocity (m/s)
H_i	Internal flow-channel pressure (MPa)	W	Flow channel width (mm)
H_j	Activation pressure threshold (MPa)	x	The flow regime index
H_{jPU}	Activation pressure threshold for PU-fitted AFE (MPa)	X	The wetted perimeter (mm)
H_{jSI}	Activation pressure threshold for SI-fitted AFE (MPa)	ΔDra	Average hourly reduction in *Dra*
H_k	Elastic restoring force of elastomer (MPa)	ΔS	The additional flow cross-sectional area induced by elastomer deformation (mm^2)
PTFE	Polytetrafluoroethylene	η	Deposited-sediment proportion (theoretically estimated, %)

1. Introduction

The Yellow River Basin spans China's arid, semiarid, and semi-humid zones. Its effective irrigated area totals 8.7 million hm^2, accounting for 12% of the national total and supporting over 30% of China's grain production (Xu 2025). Mismatched water and land resources and water scarcity impose rigid constraints on sustainable agricultural development across the basin (Kang 2021). Two major irrigation districts, Hetao (upper reaches) and Zuncun in Shanxi (middle reaches), plan to expand Yellow River water drip irrigation by $147,000$ hm^2 and $10,000$ hm^2, respectively, from 2026 to 2030. Nevertheless, Yellow River water exhibits high sediment concentrations of 3.7–26.5 kg/m^3 (Hou et al. 2024; Cheng et al. 2025). It carries abundant fine sediment particles that remain predominantly suspended and are susceptible to flocculation and adhesion (Li et al. 2016; Zhang et al. 2021). In the Heji Branch Canal of the Hetao Irrigation District, median sediment particle sizes range from 4.80 to 15.91 μm; 93.6%–97.5% of these particles can pass through the sand filters and 120-mesh (125 μm aperture) disc filters (Niu et al. 2026) and subsequently enter emitters, triggering widespread emitter clogging.

Scholars have extensively investigated sedimentation basins, filters, emitters, and pipe network flushing techniques for sediment-laden drip irrigation systems. For conventional gravity sedimentation basins, researchers have optimized inclined tube arrangements, inlet sections and overflow weirs to improve sediment removal efficiency, cutting the footprint area from 100 m^2 to 20 m^2 (Hu et al. 2020; Zha et al. 2023). Yuan et al. (2024) motorized disc compression in a disc filter and attained a sediment interception rate above 90% for 49–150 μm particles; nevertheless, the filter operated for only 4—8 min before head loss rose by 0.07

MPa. Emitters are the core components of drip irrigation systems, and low-velocity and vortex zones within flow channels primarily control emitter clogging (Tang et al. 2018; Yang et al. 2020). Numerical simulations and laboratory tests confirm that structural parameters-tooth spacing, tooth height, tooth angle, and channel depth and width-govern emitter hydraulic and anti-clogging performance (Li et al. 2006; Chen et al. 2008; Zhang et al. 2017; Xu et al. 2023). Yu et al. (2019) reported that increasing the tooth angle from 30° to 90° raised the mean in-channel flow velocity by 207.9% and reduced the fraction of particles entering vortex zones by 79%. Yang et al. (2019) rounded the sharp corners of trapezoidal flow channels, boosting turbulent kinetic energy in low—velocity zones by 52–200%. Pipe network flushing relies on hydraulic shear and scouring forces to expel sediment deposits and wall attachments from driplines (Han et al. 2018; Mo et al. 2022; Li et al. 2025), lowering the risk of clogging materials reaching emitters. Gao et al. (2025) showed that for sediment-laden water at 1 g/L, an automatic flushing valve improved the emitter flow rate by 559.5–607.1%. Even so, emitter flow rate still declined gradually under repeated flushing, because automatic flushing valves cannot remove sediments that have entered the emitter flow channels.

Although optimized emitters can mitigate sediment deposition, improve sediment discharge capacity and prolong service life to a certain degree, they are inherently limited by the fact that low-velocity and vortex zones within flow channels cannot be fully eliminated. Sediment therefore continues to accumulate on the bottom and the downstream surfaces of the teeth, gradually narrowing the flow cross-section. Accordingly, the risk of system failure from emitter clogging remains poorly controlled for long-running scenarios including subsurface drip irrigation (Mo et al. 2024), suspended drip irrigation for fruit trees (Frey et al. 2012), and

widely adopted low-flow drip irrigation systems (flow rate < 1 L/h; Yang, 2025). Furthermore, constrained by the national strategy of safeguarding the arable land red line, land suitable for sedimentation basin construction is increasingly scarce. Direct diversion of sediment-laden canal water allows over 90% of sediment to enter emitter flow channels, further elevating clogging risks. Recently, Mo et al. (2022) proposed an auto-flushing emitter (AFE): inlet pressure drives staged deformation of the elastomer, which sharply enlarges the cross-section of the flow channel and facilitates the release of trapped sediment. Gao (2023) and Niu (2024) upgraded this structure to a cylindrical AFE. Above the activation pressure threshold, its flow area expands by 0.67–131.4%, delivering 34.2–71.0% better anti-clogging performance than conventional emitters at 2 g/L sediment concentration. Yang (2025) developed a low-cost inline flat AFE and completed preliminary hydraulic tests. However, systematic research on the hydraulic variation and anti-clogging regulatory mechanisms of AFEs under sediment-laden water conditions is still lacking.

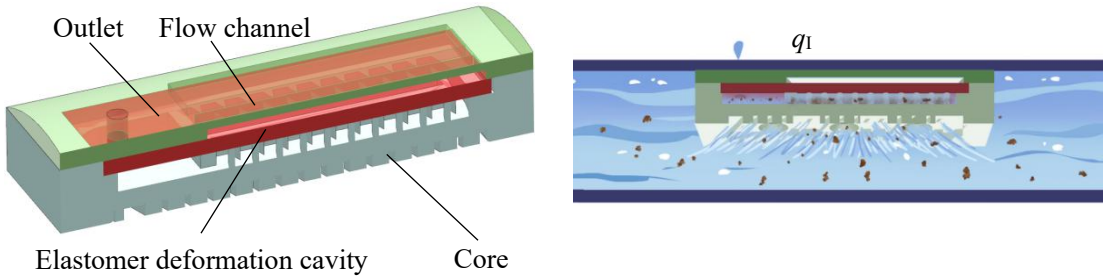
To address these issues, in this study, anti-clogging performance tests were conducted on AFEs under sediment-laden water conditions. The specific objectives were: (1) to clarify how the hydraulic performance of AFEs responds to inlet pressure and operating time under different core-elastomer combinations; (2) to identify the key controlling factors for AFE anti-clogging performance and reveal its underlying mechanisms.

2. Materials and Methods

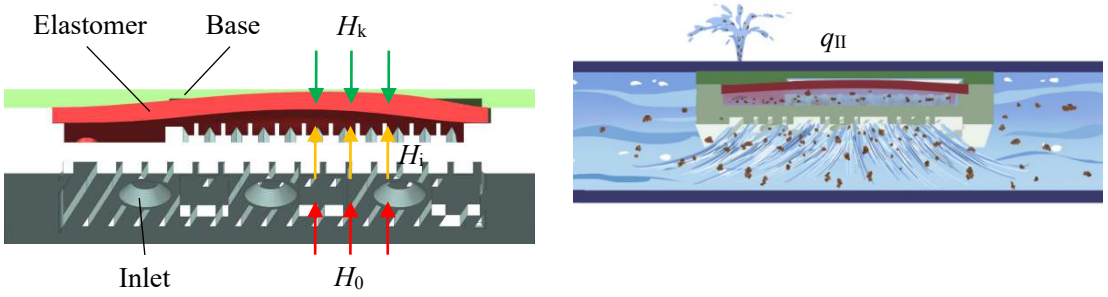
2.1 Working Principle of the auto-flushing emitter

The auto-flushing emitter (AFE) is mainly composed of a core (EMI), an elastomer, a base and an elastomer deformation cavity. The EMI is a flat part containing an inlet section, a

flow channel, and an outlet section (Fig. 1). The flat elastomer is clamped by the base and closely fitted against the outer surface of the flow channel. When the inlet pressure (H_0) is lower than the activation pressure threshold (H_j), the internal flow-channel pressure (H_i) cannot separate the elastomer away from the flow channel. Water flows only through the designed flow channel, and the AFE works under normal irrigation mode (Stage I) with an flow rate of q_I (Fig. 1a). When $H_0 > H_j$, H_i overcomes the elastic restoring force of the elastomer (H_k). The elastomer bulges into the deformation cavity and detaches from the flow channel, which results in an abrupt enlargement of the flow cross-sectional area correspondingly raises the emitter flow rate. This corresponds to the auto-flushing mode (Stage II), with a flow rate of q_{II} (Fig. 1b).



(a)



(b)

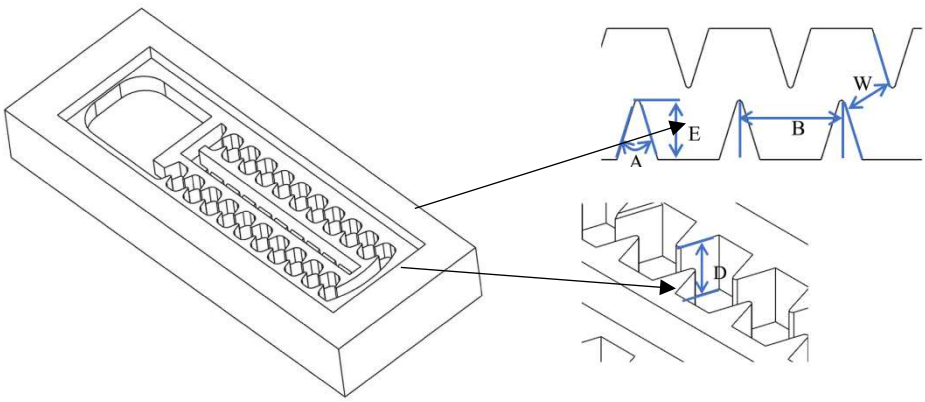
Note: H_0-inlet pressure; H_i-internal flow-channel pressure; H_k-elastic restoring force of the elastomer; q_I-AFE flow rate in normal irrigation mode;q_{II}-AFE flow rate in auto-flushing mode

Fig. 1. Cross-sectional schematics of the auto-flushing emitter (AFE) illustrating its working principle under normal irrigation mode (Stage I, a) and auto-flushing mode (Stage II, b)

2.2 Experimental Materials

2.2.1 Core

Based on the multi-objective optimization design method (OPFN) developed by our group (Yang et al. 2024), three cores (EMI1, EMI2, and EMI3) were designed with flow rates of 0.70, 0.72, and 0.95 L/h at H_0 = 0.1 MPa. Their flow-channel geometric parameters and simulated hydraulic performances are presented in Fig. 2 and Table 1. EMI1 is the pre-optimization prototype of EMI2, and the two share similar q_I. EMI1 exhibits poorer hydraulic and anti-clogging performance, with larger flow regime index (x) and structural resistance coefficient (Cs); by contrast, EMI2 achieves better performance with smaller x and Cs. All three EMIs were modeled in Unigraphics NX 12.0 and manufactured from brass via computer numerical control (CNC) precision machining to a tolerance of 0.002 mm.



Note: A-tooth angle; E-tooth height; B-tooth spacing; W-flow channel width; D-flow channel depth

Fig. 2. Schematic diagram showing the flow-channel structural parameters of the core

Table 1

Structural parameters and hydraulic performance of the tested cores

core	Structural parameters of the flow channel				Simulated hydraulic performance		
	Tooth height (mm)	Tooth angle (°)	Tooth spacing (mm)	flow channel depth (mm)	Flow rate (q_l) (L/h)	Flow regime index (x)	Structural resistance coefficient (Cs)
EMI 1	0.93	16.63	0.95	0.50	0.70	0.513	0.619
EMI 2	1.15	17.50	1.05	0.48	0.72	0.452	0.439
EMI 3	1.02	16.20	1.12	0.55	0.95	0.497	0.673

2.2.2 Elastomer

In this study, two types of elastomers, silicone (SI) and polyurethane (PU), were assembled with the three EMIs to produce six AFEs. Polytetrafluoroethylene (PTFE) was paired with the same three EMIs to fabricate three emitters as the control treatment (CK). All elastomers had a thickness of 1.0 mm, and their Shore-A hardness values were 71.5, 78.5 and 99.0 HA (Table 2).

Table 2

Experimental design

Treatment No.	Treatment		Core	Elastomer	
				Material	Shore A hardness (HA)
1–3	AFE	EMI1-SI, EMI2-SI, EMI3-SI	EMI1, EMI2, EMI3	Silicone	71.5
4–6		EMI1-PU, EMI2-PU, EMI3-PU		Polyurethane	78.5
7–9	CK	EMI1-PTFE, EMI2-PTFE, EMI3-PTFE		Polytetrafluoroethylene	99.0

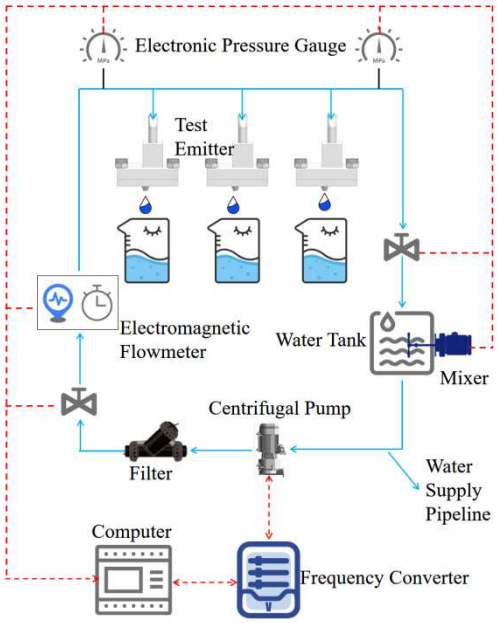
2.3 Experimental Platform

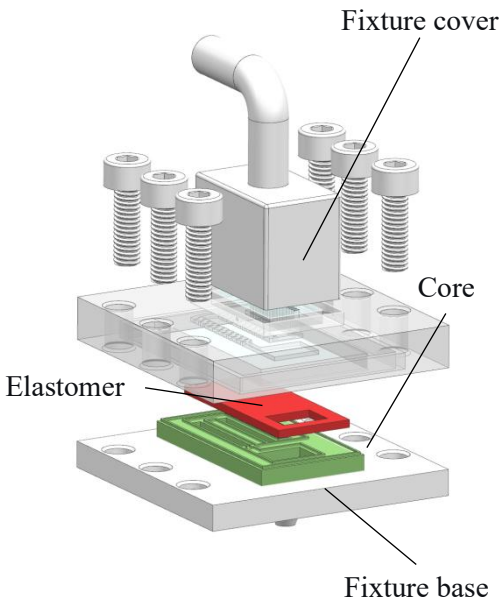
The hydraulic performance test platform was established at the National Center for Efficient Irrigation Engineering and Technology Research (Beijing).(Fig. 3) The platform was mainly composed of a computer, water tank, mixer, centrifugal pump, frequency converter, filter, pipeline, electronic pressure gauge, electromagnetic flowmeter, and test emitter. The air and water temperature were controlled by an air conditioner and a thermostat, respectively, kept at 23 ± 2 °C in accordance with GB/T 17187-2009.

The test fixture was designed by Unigraphics NX 12.0 and CNC-machined from stainless steel. It assembled the core, elastomer, fixture cover and base (Fig. 3c), and was connected to the water supply pipeline of the test platform. The target inlet pressure and measurement duration were set via the computer.



(a)





(b) (c)

Fig. 3. Hydraulic performance test platform (a), schematic layout (b), and emitter test fixture (c)

2.4 Experimental Methods

The experiments consisted of clean water (CW) and sediment-laden water (SW) tests. Each treatment was replicated three times to guarantee result reliability.

2.4.1 CW Test

Municipal tap water served as the water source. H_0 was set from 0.02 to 0.15 MPa with an increment of 0.01 MPa. The AFE flow rate (q_{CW}) of was obtained by measuring the collected water volume over 5 min.

2.4.2 SW Test

The SW test adopted the indoor short-cycle intermittent irrigation anti-clogging method reported by Niu et al. (2013). The median sediment particle size (d_{50}) was 34.84 μm (Table 3). To shorten the test period, sediment was naturally air-dried, ground, and screened with a

60-mesh sieve (aperture 0.25 mm), then mixed with tap water to prepare sediment-laden water at 2 g/L (Wang et al. 2014).

Table 3

Particle composition and incipient motion velocity of the test sediment

Particle size distribution	d_{03}	d_{10}	d_{16}	d_{25}	d_{50}	d_{75}	d_{84}	d_{90}	d_{97}
Particle size (μm)	0.72	2.88	5.58	11.42	34.84	66.82	85.05	102.80	141.70
Incipient motion velocity (m/s)	0.54–0.67	0.27–0.33	0.10–0.24	0.14–0.17	0.08–0.10	0.07–0.08	0.06–0.08	0.06–0.08	0.06–0.08

In this test, H_0 was set to 0.05, 0.10, and 0.15 MPa. The testing sequence was as follows: 1) Start the mixer to fully suspend sediment in the water tank; 2) Turn on the pump and adjust H_0 via the computer; 3) Each H_0 level ran for 30 min. The sediment-laden flow rate (q_{SW}) was sampled from 25 to 30 min during each run; 4) Stop the pump and mixer after each 30-min run, followed by a 30-min pause before the next cycle.

The test was terminated when the average relative discharge (*Dra*) fell below 75% (Eq. 2), the test was terminated. The SI, PU and PTFE groups experienced 18, 17 and 12 test cycles, corresponding to total operating times (T) of 540, 510 and 360 min, respectively (Fig. 4).



Note: -30 min off; -fitted with SI, T=30 min; -fitted with PU, T=30 min; and -fitted with PTFE, T=30 min

Fig. 4. Experimental flowchart for sediment-laden water tests

2.5 Experimental Indicators

2.5.1 Hydraulic Performance Indicators

In the CW test, the flow regime index (x) of each emitter was calculated from the q_{CW} measured at various H_0 (Eq. 1).

$$x = \frac{\sum_{i=1}^{n}(\log H_0 \log q_{CWi}) - \frac{1}{n}\sum_{i=1}^{n}(\log H_0)\sum_{i=1}^{n}(\log q_{CWi})}{\sum_{i=1}^{n}(\log H_0)^2 - \frac{1}{n}(\sum_{i=1}^{n}\log H_0)^2} \quad (1)$$

where q_{CW} is the outflow rate (L/h), H_0 is the inlet pressure (MPa), n is the number of pressure

175 levels (n=6), and i its the sequence number of H_0.

176 **2.5.2 Average Relative Discharge**

177 In the SW test, the average relative discharge (*Dra*) of each emitter was calculated as the

178 ratio of q_{SW} to the corresponding q_{CW} measured at the same H_0 (Eq. 2). A higher *Dra* indicates

179 better anti-clogging performance, and the emitter was considered clogged when *Dra* fell

180 below 75% (BS 7605-2, 1992).

$$Dra = \frac{q_{SW}}{q_{cw}} \times 100\% \quad (2)$$

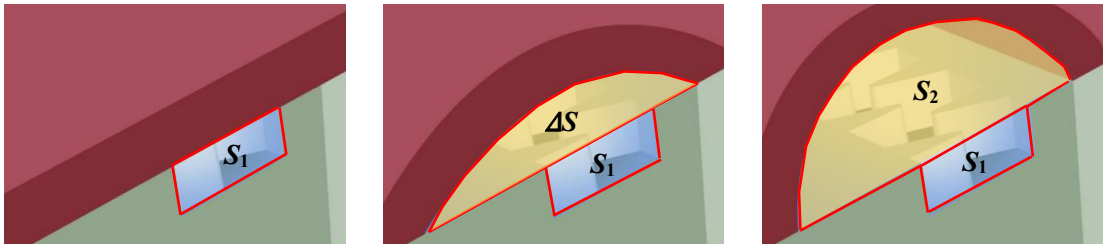
181 **2.5.3 Flow Cross-sectional Area of the Emitter**

182 In this study, sediment deposition within the emitter flow channel was evaluated by

183 comparing the cross-sectional average flow velocity (v) with the incipient motion velocity of

184 sediment particles (U_c) (Table 3). This required calculating the flow cross-sectional area (S) of

185 each AFE under different H_0 (Fig.5).



(a) (b) (c)

Note: Blue-original channel cross-section; Yellow-additional flow channel cross-section

Fig. 5. Opening configurations of the emitter flow channel under different inlet pressures

186 For the AFE, SI and PU were assumed non-deformable when $H_0 \leq H_j$, so S equaled the

187 original channel cross-sectional area (S_1) (Fig.5a). When $H_0 > H_j$, both SI and PU underwent

188 deformation (Fig.5b); thus S was the sum of S_1 and the additional cross-sectional area induced

by elastomer deformation (ΔS) (Eq. 3). At H_0 = 0.15 MPa, SI was regarded as fully deformed and compressed against the base (Fig.5c), yielding an additional cross-sectional area S_2 where $\Delta S = S_2$. Eq. 4 calculates ΔS for the SI-fitted AFE at H_0 = 0.10 MPa, as well as for PU-fitted H_0 = 0.10 MPa and H_0 = 0.15 MPa. For PU-fitted AFEs, ΔS was derived by multiplying the ΔS of SI-fitted AFE by the Shore A hardness ratio of SI to PU. For CK, ΔS was taken as zero across the tested H_0 range of 0.05–0.15 MPa.

$$S = S_1 + \Delta S \tag{3}$$

$$\Delta S = \begin{cases} S_2 \times \dfrac{0.10 - H_{\mathrm{jSI}}}{0.15 - H_{\mathrm{jSI}}}, & \text{The elastomer is SI} \\ S_2 \times \dfrac{0.10 - H_{\mathrm{jSI}}}{0.15 - H_{\mathrm{jSI}}} \times \dfrac{SS_{\mathrm{SI}}}{SS_{\mathrm{PU}}}, & \text{The elastomer is PU} \end{cases} \tag{4}$$

where S is the flow cross-sectional area (mm^2); S_1 is the original flow channel cross-sectional area (mm^2), measurable via Unigraphics NX 12.0; ΔS is the additional flow cross-sectional area induced by elastomer deformation (mm^2); S_2 is the value of ΔS when SI is fully deformed and compressed against the base at H_0 = 0.15 MPa (mm^2), also measurable in Unigraphics NX 12.0; H_{jSI} is the activation pressure threshold for the SI-fitted AFE, with values of 0.08, 0.07, and 0.07 MPa for EMI1-SI, EMI2-SI, and EMI3-SI, respectively; SS_{SI} is the Shore A hardness of SI (71.5 HA); and SS_{PU} is the Shore A hardness of PU (78.5 HA).

The wetted perimeter (X) of the flow cross-section was measured using Unigraphics NX 12.0, and the hydraulic radius (h) was calculated via Eq. 5.

$$h = \frac{S}{X} \tag{5}$$

The v for each AFE under varying H_0 is given in Eq. 6.

$$v = \frac{q_{CW}}{S} \tag{6}$$

Based on the findings reported by Qian et al. (2003) (Eq. 7), sediment particles were assumed to remain unentrained and not transported by the flow when $v < U_c$. The ratio between the mass fraction of such sediment and the total sediment mass was defined as the deposited-sediment proportion (η). A higher η indicates a greater risk of emitter clogging.

$$U_c = \left[0.43 d^{3/4} + 1.1 \frac{(0.7-\varepsilon)^4}{d} \right]^{1/2} h^{1/5} \tag{7}$$

Where U_c is the incipient motion velocity of sediment particles (m/s); d is the sediment particle size (mm) (see Table 3); ε is the porosity, set to 0.4; and h is the hydraulic radius (m).

2.7 Data Processing

Analysis of variance (ANOVA) was performed with EMI type, elastomer material, and H_0 set as fixed factors to examine their effects on emitter *Dra*. The least-significant-difference (LSD) test at $P < 0.05$ applied for multiple comparisons among mean values of the measured indicators. All statistical analyses were performed using the statsmodels library (v0.14.6) in Python 3.9.7.

3. Results and Analysis

3.1 Hydraulic Performance of Emitters in the CW Test

For CK emitters fitted with PTFE, q_{CW} did not increase step-wise with rising H_0. At H_0 = 0.10 MPa, q_{CW} for EMI1-PTFE, EMI2-PTFE, and EMI3-PTFE were 0.72, 0.71, and 0.97 L/h,with corresponding x were 0.503, 0.440, and 0.502, respectively (Fig. 6). By contrast, q_{CW} of AFEs fitted with SI and PU increased step-wise as H_0 rose. The H_j was 0.08 MPa for EMI1-SI and 0.09 MPa for EMI1-PU; 0.07 MPa for EMI2-SI and 0.08 MPa for EMI2-PU;

and 0.07 MPa for EMI3-SI and 0.10 MPa for EMI3-PU.

The q_{CW}-H_0 for emitters fitted with different elastomers nearly overlapped when $H_0 < H_j$. Above H_j, q_{CW} of the AFEs increased linearly with H_0; SI-fitted AFEs exhibited larger growth in q_{CW} than PU-fitted counterparts, and this disparity widened as q_{CW} increased. At H_0 = 0.15 MPa, q_{CW} of EMI1-SI was 2.6% and 46.3% higher than EMI1-PU and EMI1-PTFE, respectively; EMI2-SI was 6.3 % and 49.5 % higher than EMI2-PU and EMI2-PTFE; and EMI3-SI was 17.6 % and 44.0 % higher than EMI3-PU and EMI3-PTFE.

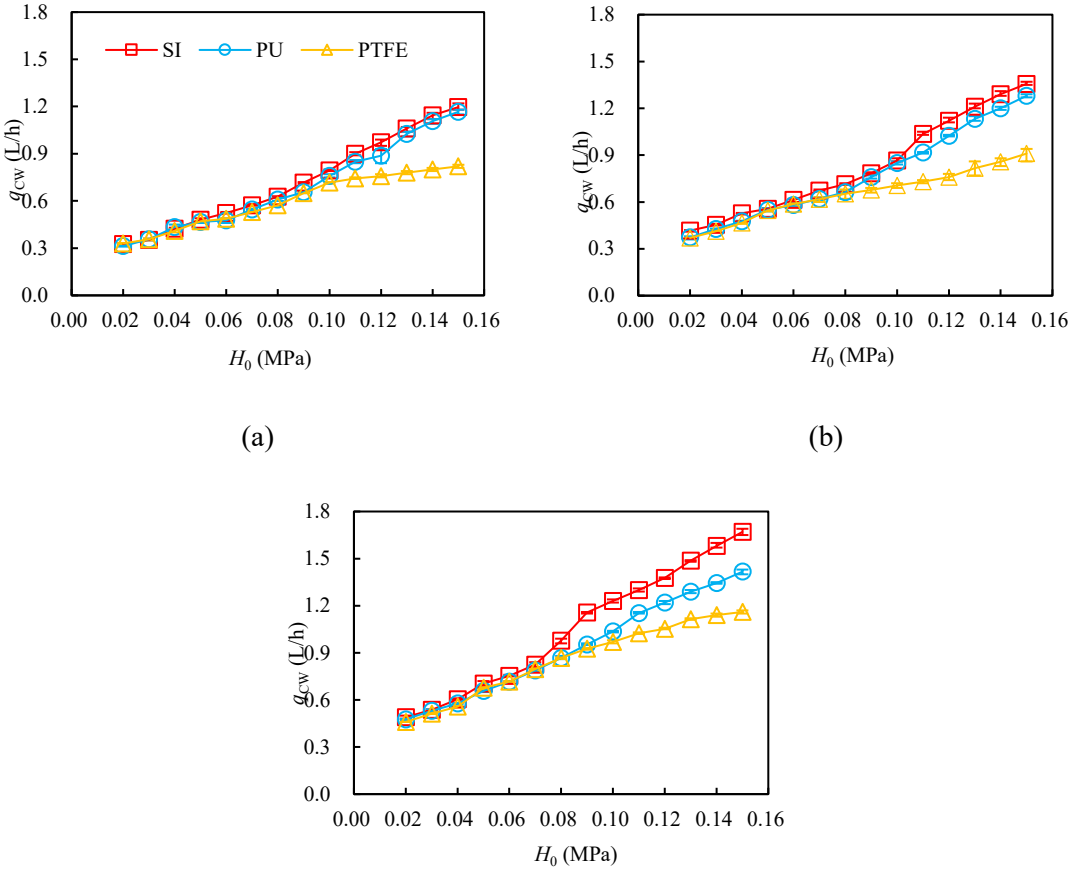


Fig. 6. Variation in emitter flow rate (q_{CW}) with inlet pressure (H_0) under clean-water conditions for EMI1 (a), EMI2 (b), and EMI3 (c) fitted with silicone (SI), polyurethane (PU), and polytetrafluoroethylene (PTFE), respectively

3.2 Hydraulic Performance of Emitters in the SW Test

During the SW test, *Dra* declined with increasing *T* for all nine treatments. For AFEs, the magnitude of this *Dra* reduction weakened as H_0 rose; by contrast, CKs exhibited no clear dependence of decline on H_0 (Fig. 7).

For SI-fitted AFEs, the *Dra*-*T* curves of the three structures largely overlapped at H_0 = 0.05 and 0.15 MPa. At H_0 = 0.05 MPa, *Dra* of all three AFEs fell to the 75% threshold at *T* = 270 min. At H_0 = 0.10 MPa, EMI1-SI showed a more rapid drop in *Dra* than the other two; its *Dra* reached 75% at *T* = 390 min, while EMI2-SI and EMI3-SI stayed above 75% until the test ended (*T* = 540 min). At H_0 = 0.15 MPa, *Dra* of all three SI-fitted AFEs remained above 75% throughout the test.

For PU-fitted AFEs, the overall *Dra* reductions of the three emitters were comparable at H_0 = 0.05 and 0.10 MPa by the test endpoint (*T* = 510 min). At H_0 = 0.05 MPa, *Dra* of EMI1-PU and EMI3-PU dropped to 75% between 180 and 210 min, whereas EMI2-PU reached this threshold at *T* = 240 min. At H_0 = 0.10 MPa, EMI1-PU and EMI3-PU hit 75% between 270 and 300 min, while EMI2-PU reached 75% at *T* = 390 min.

For PTFE-fitted CKs, the three emitters exhibited similar *Dra* decay trends over time at H_0 = 0.05 MPa, yielding a mean *Dra* of 65.8% at the end of the test (*T* = 360 min). At H_0 = 0.10 and 0.15 MPa, the EMI1-PTFE reached an average *Dra* of 64.9% at *T* = 360 min, while the EMI2-PTFE and EMI3-PTFE attained 71.8% and 72.4%, corresponding to 10.6% and 11.6% higher values than the EMI1-PTFE.

At *T* = 360 min, the SI-fitted AFEs achieved higher *Dra* than PU-fitted and PTFE-fitted emitters: increments of 8.8% and 2.0% at H_0 = 0.05 MPa; 11.5% and 17.3% at H_0 = 0.10 MPa;

and 14.2% and 30.2% at H_0 = 0.15 MPa.

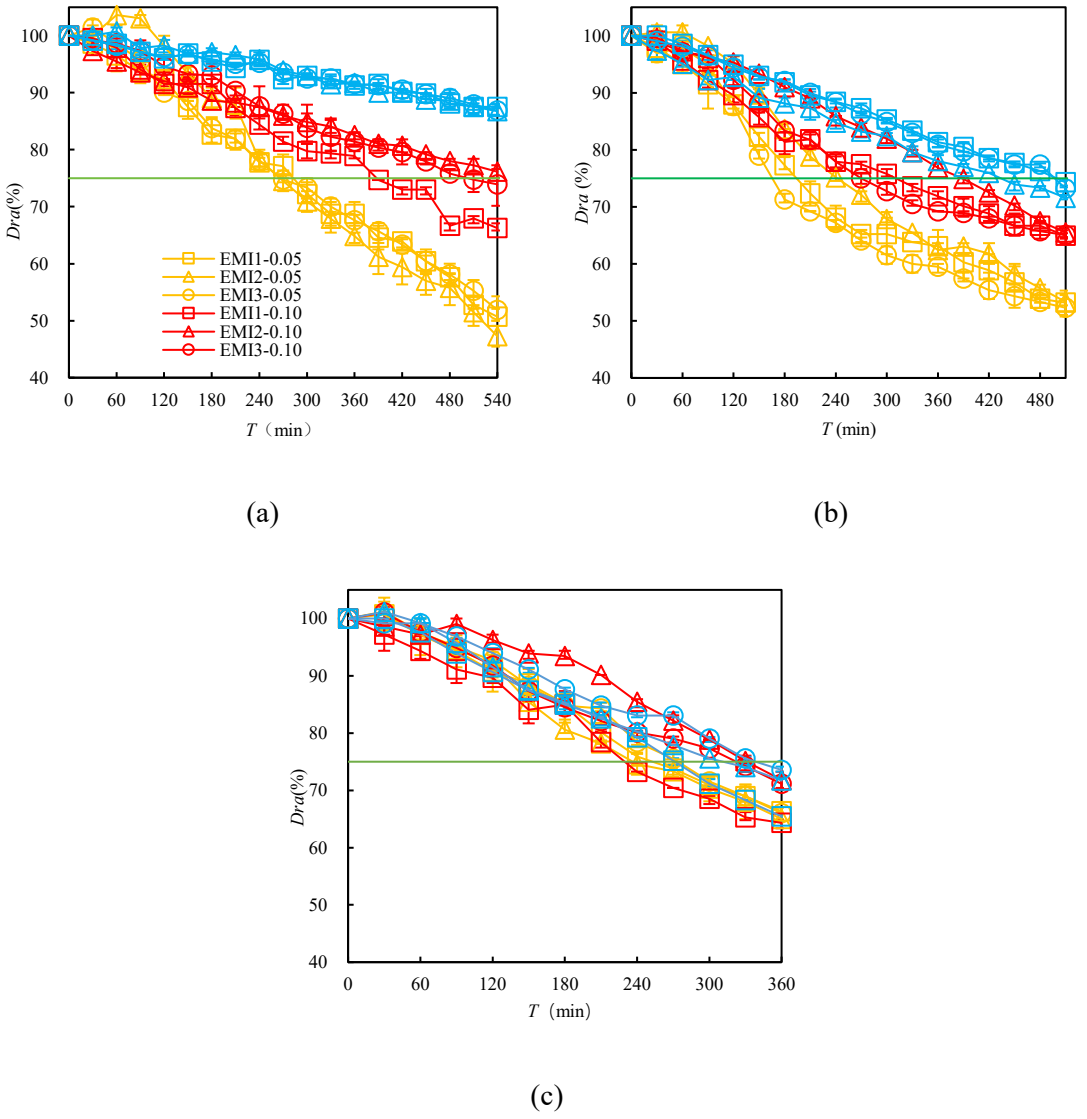


Fig. 7. Variation in average relative discharge (*Dra*) with operating time (*T*) at inlet pressures of 0.05, 0.10, and 0.15 MPa for emitters fitted with (a) silicone (SI), (b) polyurethane (PU), and (c) polytetrafluoroethylene (PTFE) under the SW test

A smaller average hourly reduction in *Dra* (Δ*Dra*) indicates stronger anti-clogging performance of the emitter. Except for EMI1-PTFE and EMI2-PTFE, Δ*Dra* declined as H_0 increased, with significant differences across the three H_0 levels ($P < 0.05$) (Table 4). For the remaining seven emitter groups, raising H_0 from 0.05 MPa to 0.10 MPa and 0.15 MPa

reduced Δ*Dra* from 5.34–5.86% to 2.65–4.81% and 1.39–4.41%, respectively.

Δ*Dra* for all nine treatments generally decreased with declining Shore A hardness of the elastomer. As Shore A hardness fell from 99.0 HA (PTFE) to 78.5 HA (PU) and 71.5 HA (SI), Δ*Dra* decreased from 4.96–5.77%% to 4.22–4.30% and 3.23–3.54%, respectively. For EMI1 and EMI2, the mean Δ*Dra* of SI-fitted AFEs significantly reduced by 36.5% relative to that of PTFE-fitted counterparts ($P < 0.05$). For EMI3, the mean Δ*Dra* of SI- and PU-fitted AFEs was significantly reduced by 34.9% and 13.5%, respectively, relative to the PTFE-fitted group ($P < 0.05$).

For identical H_0 and elastomer material, the average Δ*Dra* of the three EMI types followed EMI1 > EMI2 > EMI3. The average Δ*Dra* of EMI1 was 5.99% and 7.76% higher than EMI2 and EMI3, respectively, but the differences were not significant ($P > 0.05$). The ANOVA results indicated that EMI type, elastomer material, H_0, their two-way interactions, and the three-way interaction significantly affected Δ*Dra* ($P < 0.05$).

Table 4

Significance analysis of the average hourly decrease in average relative discharge (Δ*Dra*) of emitters in the SW test

Treatment	H_0 (MPa)	Treatment	Δ*Dra* (%)
EMI1-SI	0.05	EMI1-SI-0.05	5.48±0.14 a
	0.10	EMI1-SI-0.10	3.75±0.08 b
	0.15	EMI1-SI-0.15	1.39±0.46 c
	Mean		3.54 A
EMI1-PU	0.05	EMI1-PU-0.05	5.51±0.20 a
	0.10	EMI1-PU-0.10	4.13±0.16 b

Treatment	H_0 (MPa)	Treatment	ΔDra (%)
	0.15	EMI1-PU-0.15	3.02±0.06 c
	Mean		4.22 B
EMI1-PTFE	0.05	EMI1-PTFE-0.05	5.61±0.10 a
	0.10	EMI1-PTFE-0.10	5.95±0.13 ab
	0.15	EMI1-PTFE-0.15	5.76±0.12 b
	Mean		5.77 B
	Mean		4.51 $
EMI2-SI	0.05	EMI2-SI-0.05	5.86±0.2 a
	0.10	EMI2-SI-0.10	2.65±0.13 b
	0.15	EMI2-SI-0.15	1.47±0.12 c
	Mean		3.33 A
EMI2-PU	0.05	EMI2-PU-0.05	5.49±0.12 a
	0.10	EMI2-PU-0.10	4.06±0.08 b
	0.15	EMI2-PU-0.15	3.34±0.05 c
	Mean		4.30 AB
EMI2-PTFE	0.05	EMI2-PTFE-0.05	5.83±0.17 a
	0.10	EMI2-PTFE-0.10	4.69±0.24 a
	0.15	EMI2-PTFE-0.15	4.72±0.11 b
	Mean		5.08 B
	Mean		4.24 $
EMI3-SI	0.05	EMI3-SI-0.05	5.34±0.24 a
	0.10	EMI3-SI-0.10	2.90±0.37 b
	0.15	EMI3-SI-0.15	1.46±0.09 c
	Mean		3.23 A
EMI3-PU	0.05	EMI3-PU-0.05	5.61±0.18 a
	0.10	EMI3-PU-0.10	4.11±0.07 b

Treatment	H_0 (MPa)	Treatment	ΔDra (%)
	0.15	EMI3-PU-0.15	3.15±0.05 c
		Mean	4.29 AB
EMI3-PTFE	0.05	EMI3-PTFE-0.05	5.67±0.17 a
	0.10	EMI3-PTFE-0.10	4.81±0.17 b
	0.15	EMI3-PTFE-0.15	4.41±0.08 c
		Mean	4.96 B
	Mean		4.16 $
F test for EMI		39.679 (***)	
F test for elastomer		1041.780 (***)	
F test for H_0		1707.040 (***)	
F test for EMI*elastomer		21.846 (***)	
F test for EMI* H_0		25.023 (***)	
F test for elastomer*H_0		274.782 (***)	
F test for EMI*elastomer*H_0		12.382 (***)	

Note: For a given EMI and elastomer, different lowercase letters denote significant differences in ΔDra among inlet pressures (H_0) at $P < 0.05$. For a given EMI, different uppercase letters indicate that the mean ΔDra averaged across the three H_0 levels differs significantly among elastomers at $P < 0.05$. The same symbol ($) denotes no significant difference in the overall mean ΔDra (averaged across the three H_0 levels and three elastomers) among EMI types at $P < 0.05$. *, **, and *** indicate significance at $P < 0.05$, $P < 0.01$, and $P < 0.001$, respectively.

3.3 Estimation of sediment deposition in emitter flow channels

For water conveyance in canals and large-diameter pipelines, the flow-sediment interaction governs sediment incipient motion and transport (Dey et al. 2008). Sediment

entrainment depends on whether the hydrodynamic drag and lift forces from the flow are large enough to overcome the submerged weight of particles and bed cohesive resistance. This threshold condition is commonly described by the U_c. Sediment particles start to move only when the v exceeds U_c (Tang et al. 2023; Sun et al. 2025; Shen et al. 2026).

For AFEs, S, X and h increased with rising H_0, while v tended to decrease. By contrast, v of CKs increased with H_0. As H_0 increased from 0.05 MPa to 0.10 MPa and 0.15 MPa, the mean S of AFEs increased by 76.9% and 220.8%, mean X increased by 27.3% and 78.2%, and mean v decreased by 7.4% and 25.5%, respectively. For CKs, mean v increased by 40.2% and 69.1% (Table 5). At H_0 of 0.05, 0.10 and 0.15 MPa, U_c of the test sediment in the nine emitter flow channels ranged from 0.07 m/s to 0.70 m/s, and U_c for the d_{50} sediment was 0.09–0.11 m/s. At the end of the test, η of AFEs, estimated using U_c and v, was 7.90%–26.13%, while η of CKs ranged from 0 to 9.40%. As H_0 increased, η of AFEs gradually increased, whereas η of CKs gradually decreased.

When fitted with SI and PU elastomers, EMI1 and EMI2 had similar η values at H_0 = 0.05 MPa, with an average of 9.29%, while the average η of EMI3 was 12.12% lower. At H_0 = 0.10 MPa, η of EMI1 and EMI2 was 9.72% and 13.57%, respectively; η of EMI3 was 6.64% and 33.16% lower than EMI1 and EMI2, respectively. At H_0 = 0.15 MPa, η of AFEs ranged from 12.11% to 26.13%, which were 87.42% and 54.83% greater than those at H_0 = 0.05 MPa and 0.10 MPa.

For PTFE-fitted CKs, the average η of the three CKs was 8.96% at H_0 = 0.05 MPa, and η of EMI3-PTFE was 12.45% and 13.16% lower than EMI1-PTFE and EMI2-PTFE, respectively. As H_0 rose from 0.05 to 0.10 MPa, η of EMI1 and EMI2 decreased to 5.24% and

306 7.19%, and η of EMI3 decreased to 4.38%. When H_0 further increased to 0.15 MPa, η of

307 EMI1 and EMI2 dropped to 3.60% and 4.42%; for EMI3, v exceeded U_c for all sediment

308 particle sizes, and its η decreased to 0.

309 **Table 5**

310 Hydraulic characteristics and clogging status of the nine emitter types at three inlet pressures

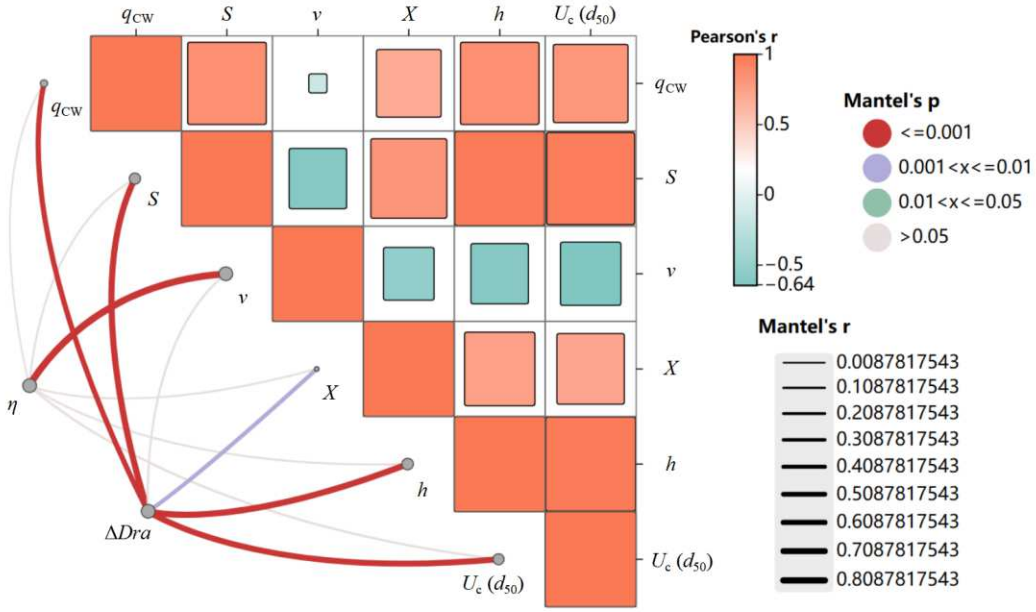
Treatment	H_0 (MPa)	q_{CW} (L/h)	S (mm^2)	v (m/s)	X (mm)	h (mm)	U_c (m/s)		η (%)	ΔDra (%)
							d_{03}–d_{97}	d_{50}		
EMI1-SI	0.05	0.48	0.39	0.34	2.47	0.16	0.07–0.61	0.09	9.16	5.48
	0.10	0.79	0.65	0.34	3.06	0.21	0.07–0.65	0.10	9.72	3.75
	0.15	1.20	1.30	0.26	4.51	0.29	0.08–0.69	0.11	15.51	1.39
EMI2-SI	0.05	0.56	0.45	0.34	2.70	0.17	0.07–0.62	0.09	9.26	5.86
	0.10	0.87	0.88	0.28	3.57	0.25	0.08–0.67	0.10	13.79	2.65
	0.15	1.36	1.59	0.24	5.01	0.32	0.08–0.70	0.11	17.77	1.47
EMI3-SI	0.05	0.7	0.48	0.41	2.73	0.18	0.07–0.62	0.10	7.90	5.34
	0.10	1.23	0.85	0.40	3.53	0.24	0.08–0.67	0.10	8.58	2.90
	0.15	1.67	1.48	0.31	4.85	0.30	0.08–0.70	0.11	12.11	1.46

Treatment	H_0 (MPa)	q_{CW} (L/h)	S (mm^2)	v (m/s)	X (mm)	h (mm)	U_c (m/s)		η (%)	ΔDra (%)
							d_{03}–d_{97}	d_{50}		
EMI1-PU	0.05	0.47	0.39	0.34	2.47	0.16	0.07–0.61	0.09	9.32	5.51
	0.10	0.76	0.63	0.34	3.00	0.21	0.07–0.65	0.10	9.71	4.13
	0.15	1.17	1.22	0.27	4.33	0.28	0.08–0.69	0.11	14.80	3.02
EMI2-PU	0.05	0.55	0.45	0.34	2.70	0.17	0.07–0.62	0.09	9.40	5.49
	0.10	0.85	0.84	0.28	3.49	0.24	0.08–0.67	0.10	13.35	4.06
	0.15	1.28	1.49	0.24	4.80	0.31	0.08–0.70	0.11	26.13	3.34
EMI3-PU	0.05	0.66	0.48	0.38	2.73	0.18	0.07–0.62	0.10	8.42	5.61
	0.10	1.04	0.82	0.35	3.46	0.24	0.08–0.66	0.10	9.56	4.11
	0.15	1.42	1.39	0.28	4.66	0.30	0.08–0.69	0.11	13.87	3.15
EMI1-PTFE	0.05	0.47	0.39	0.34	2.47	0.16	0.07–0.61	0.09	9.32	5.61
	0.10	0.72	0.39	0.51	2.47	0.16	0.07–0.61	0.09	5.24	5.95

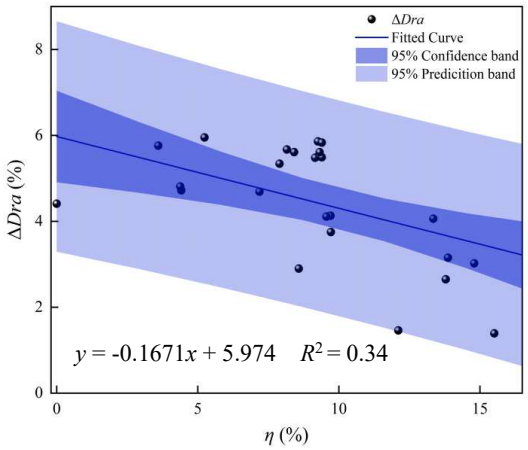
Treatment	H_0 (MPa)	q_{CW} (L/h)	S (mm^2)	v (m/s)	X (mm)	h (mm)	U_c (m/s)		η (%)	ΔDra (%)
							d_{03}–d_{97}	d_{50}		
	0.15	0.82	0.39	0.58	2.47	0.16	0.07–0.61	0.09	3.60	5.76
EMI2-PTFE	0.05	0.55	0.45	0.34	2.70	0.17	0.07–0.62	0.09	9.40	5.83
	0.10	0.71	0.45	0.43	2.70	0.17	0.07–0.62	0.09	7.19	4.69
	0.15	0.91	0.45	0.56	2.70	0.17	0.07–0.62	0.09	4.42	4.72
EMI3-PTFE	0.05	0.68	0.48	0.39	2.73	0.18	0.07–0.62	0.10	8.16	5.67
	0.10	0.97	0.48	0.56	2.73	0.18	0.07–0.62	0.10	4.38	4.81
	0.15	1.16	0.48	0.67	2.73	0.18	0.07–0.62	0.10	0.00	4.41

3.4 Correlation and regression analysis of hydraulic and anti-clogging indicators

Pearson correlation analysis showed that q_{CW}, S, and h had strong positive correlations with $U_c(d_{50})$, while v was moderately negatively correlated with these parameters (Fig. 8a). X exhibited weak-to-moderate positive correlations with q_{CW}, S, h and $U_c(d_{50})$, but was negatively correlated with v. The Mantel test further quantified the responses of anti-clogging indicators ΔDra and η to emitter hydraulic parameters. ΔDra was significantly correlated with q_{CW}, S, X, h, and $U_c(d_{50})$, whereas η was significantly correlated only with v. Linear fitting between ΔDra and η (note that η is theoretically derived rather than directly measured) yielded a moderate negative correlation (R^2 = 0.34) with a narrow 95% confidence interval, supporting reliable overall trend estimation (Fig. 8b). By contrast, the 95% prediction interval was much wider, indicating large scatter in clogging responses at a given η. Accordingly, η and ΔDra do not follow a strict linear relationship, and η alone cannot adequately characterize emitter anti-clogging performance.



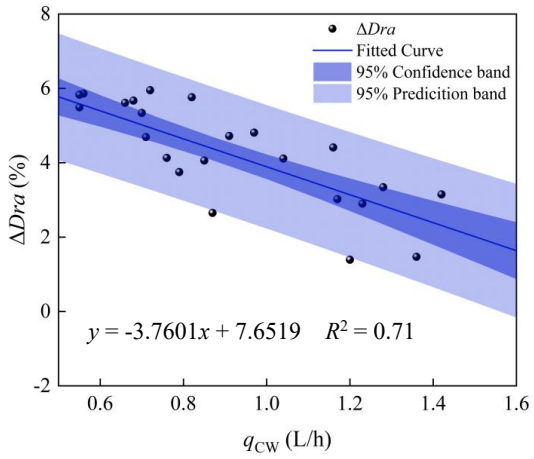
(a)



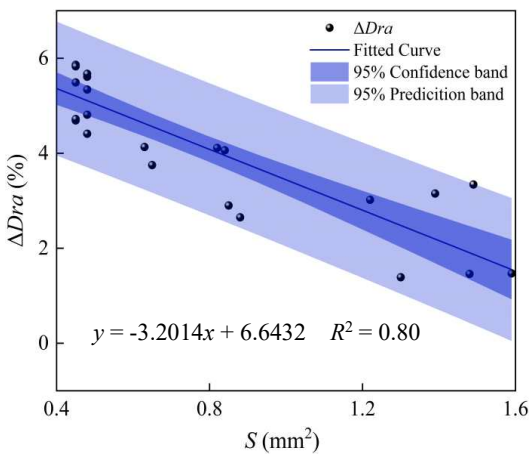
(b)

Fig. 8. Correlation matrix of emitter test indicators (a) and the relationship between anti-clogging indicators (b)

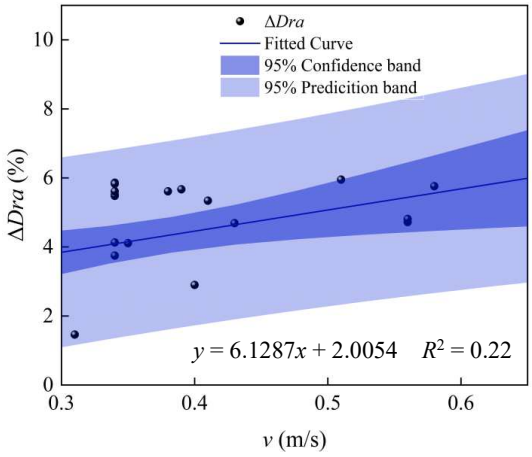
To further quantify the independent effects of emitter parameters on anti-clogging performance, univariate linear regression models were constructed with q_{CW}, S, and v as independent variables and ΔDra as the dependent variable (Fig. 9). Both S and q_{CW} were strongly negatively correlated with ΔDra and were the dominant factors affecting emitter anti-clogging performance (R^2 = 0.71–0.80). Although v was positively correlated with ΔDra, the linear correlation was weak (R^2 = 0.22), indicating that its clogging effect must be evaluated together with S.



(a)



(b)



(c)

Fig. 9. Relationship between ΔDra of emitters and (a) q_{CW}, (b) S, and (c) v

4 Discussion

4.1 Effects of EMI and Elastomer on the Hydraulic Performance of Emitters

The AFE operates in two modes: normal irrigation (Stage I) and auto-flushing (Stage II). The transition is driven by the H_i, which rises with increasing H_0; when H_i exceeds the activation threshold H_j, the AFE switches from Stage I to Stage II (Mo et al. 2022). Under a given H_0, the outlet pressure of the flow channel is zero, so the head loss per unit length is identical across emitters, and H_i at any given channel position is the same. With an identical elastomer (i.e., the same H_k), the magnitude of stress-induced deformation is similar. Accordingly, H_j ranged from 0.07 to 0.08 MPa for the three SI-fitted AFEs and from 0.08 to 0.10 MPa for the PU-fitted AFEs. Because H_k decreases with declining Shore A hardness (Wang, 2022), H_j follows the same trend; indeed, H_j of the SI-fitted AFEs was on average 18.5% lower than that of the PU-fitted AFEs. Gao (2023) and Niu (2024) achieved auto-flushing by wrapping the elastomer around the outer surface of the EMI in a cylindrical form, which differs from the flat configuration adopted here. Nevertheless, their conclusion that H_j decreases with lower elastomer Shore A hardness and thickness is consistent with the

present results.

4.2 Variation in Hydraulic Performance of Emitters without Auto-flushing under Sediment-laden Water

In this study, PTFE-fitted emitters without auto-flushing function showed hydraulic characteristics similar to conventional non-pressure-compensating emitters (NPCs). Previous studies have demonstrated that the clogging progression of NPCs is highly sensitive to sediment properties, sediment concentration, operational regime and emitter nominal flow rate. For instance, under Yellow River water irrigation, NPCs exhibited markedly different times to reach *Dra* = 75%: Ma et al. (2024) and Shen et al. (2022) reported 300–560 h in Hetao Irrigation District (0.041–0.41 g/L, d_{50}=10.1 μm); Xiang (2024) obtained a much shorter duration of 4.3–5.6 h in Zuncun Irrigation District under higher sediment concentrations (1.0–4.0 g/L, d_{50} = 30–50 μm) with intermittent 20 min on–30 min off cycles. Ren et al. (2024) observed a range of 8–32 h using coarser floodplain sand (d_{50}=42.7–82.4 μm, 1–3 g/L). Longer lifespans of 144–355 h were found for emitters tested with Shihezi sediment (d_{50}=180–212 μm, 3 g/L; Xing et al. 2025), while Zhu et al. (2025) reported failure after 19 h of continuous operation with high-concentration red-soil suspension (5.0 g/L, d_{50}=36.46 μm). In our intermittent test (30 min on–30 min off, 2 g/L, d_{50}=34.84 μm), the *Dra* of emitters (q_{CW} = 0.70–0.95 L/h) decreased to 75% within 4–6 h. This decay trend agreed well with Xiang (2024), consistent with the shared intermittent operation scheme. Overall, divergences across studies can be attributed to differences in sediment characteristics, inlet sediment concentration, cyclic operation patterns and emitter flow rate.

Based on the OPFN method of Yang et al. (2024), which integrates indicators such as *x*

and *Cs*, the flow-channel geometry of EMI1 was optimized to yield EMI2. The SW test showed that, relative to EMI1-PTFE, EMI2-PTFE at T = 360 min exhibited a 6.38% higher *Dra*, a 26.47% longer time to reach *Dra* = 75%, and a lower Δ*Dra*, indicating improved anti-clogging performance. Although q_{CW} and v of EMI1-PTFE were close to those of EMI2-PTFE, the OPFN-optimized geometry enhanced scouring by expanding the high-velocity, high-turbulent-kinetic-energy zones in the mainstream region and reducing the low-velocity, low-turbulent-kinetic-energy zones near the tooth bottom and downstream face, thereby lowering sediment-deposition risk (Dallagi et al. 2024; Yang et al. 2024; Wang et al. 2025).

4.3 Anti-clogging Performance of AFEs under Sediment-laden Water

Optimization of the flow channel structure improved the anti-clogging performance of EMI2-PTFE by 14.76–18.61% relative to EMI1-PTFE, although clogging still gradually occurred with increasing operating time T. When fitted with the SI elastomer and operated at $H_0 > H_j$, EMI2-SI exhibited a further improvement of 47.09–70.06% in anti-clogging performance. At the same T, compared with the CKs and AFEs operating in Stage I (normal irrigation, H_0 = 0.05 MPa), the six AFEs (EMI1-SI, EMI2-SI, EMI3-SI, EMI1-PU, EMI2-PU, EMI3-PU) tested at H_0 of 0.10 and 0.15 MPa achieved a 16.38–54.20% higher *Dra*, while their Δ*Dra* decreased significantly by 30.63–74.06% and 5.63–78.64%. Such performance differences increased with rising H_0 and declined as the Shore A hardness of the elastomer decreased.

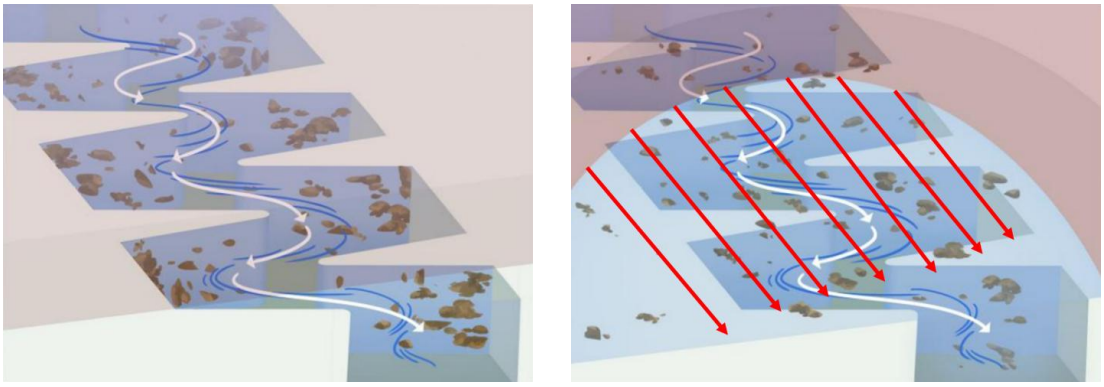
Although the ANOVA indicated that core type exerted a significant overall effect on Δ*Dra*, no significant pairwise differences were detected among EMI1, EMI2 and EMI3

390 (Table 4). This suggests that core-driven differences in anti-clogging performance were
391 modulated by strong interactions with elastomer material and H_0.

392 **4.4 Mechanism Underlying the Auto-flushing Anti-clogging Behaviour of AFEs**

393 For SI-fitted AFEs in this study, the SI remained undeformed at H_0 = 0.05 MPa and
394 became fully deformed and pressed against the base at H_0 = 0.15 MPa. Using H_{jSI}, H_{jPU}, SS_{SI},
395 and SS_{PU}, we calculated S and X for SI- and PU-fitted AFEs under the three H_0 and further
396 derived v and U_c. Both S and q_{CW} increased with H_0, yet S exhibited a larger relative
397 increment with rising H_0. As a result, v generally decreased as H_0 increased. Specifically,
398 when H_0 rose from 0.05 MPa to 0.10 MPa and 0.15 MPa, the v of AFEs decreased by 7.54%
399 and 25.47%, respectively.

400 In open channels and large-diameter pipelines, sediment deposition is usually judged by
401 comparing v and U_c (Dey et al. 2008; Li et al. 2018; Archibong-Eso et al. 2020; Gong et al.
402 2021). When this criterion was applied to the emitter flow channels, η of AFEs increased with
403 H_0 and decreased with higher Shore A hardness, which was opposite to the trend of ΔDra:
404 ΔDra decreased with increasing H_0 and increased with Shore A hardness. Under
405 sediment-laden water, v serves as the basic driving force for sediment movement, yet for
406 these emitters with narrow flow cross-sections (S = 0.39–1.59 mm^2), S acts as the primary
407 factor controlling smooth sediment discharge (Fig. 10). Liu et al. (2018) reported a similar
408 finding, showing that emitter clogging time was positively correlated with flow channel
409 cross-sectional size.



(a) (b)

Note: Blue lines-water flow within the flow channel; white lines-velocity streamlines in the fixed flow channel; red lines-velocity streamlines in the additional expanded flow channel

Fig. 10. Sediment deposition characteristics in the flow channel before and after switching to the auto-flushing mode (cross-sectional area expansion)

Pearson correlation and regression analysis further demonstrated that, for sediment particles ranging from 0.72 to 141.70 μm at a sediment concentration of 2 g/L, ΔDra of AFEs had strong linear negative correlations with S and q_{CW} (R^2=0.710–0.8079), whereas the correlation with η and v was weak. These results reveal the core anti-clogging mechanism of the AFE: increasing H_0 enlarges S, which expands the cross-section available for sediment evacuation and substantially improves anti-clogging capacity. Aminpour et al. (2022) tested three types of pressure-compensating emitters with different self-cleaning structures and found that their anti-clogging performance depended on flow patterns and channel cross-section dimensions associated with self-cleaning components. This agrees well with our conclusion that S dominates sediment transport and determines emitter anti-clogging performance.

This finding provides reference data for the operation of drip irrigation systems using sediment-laden water. When emitter outflow drops substantially, the water supply pressure

can be increased periodically to drive further elastomer deformation, switching the AFE from Stage I (normal irrigation) to Stage II (auto-flushing). The enlarged flow cross-section facilitates sediment removal, enabling periodic auto-flushing and clogging mitigation. Nevertheless, this study was conducted under laboratory controlled conditions, with limited representation of complex field boundary conditions such as variable sediment grading, unsteady water supply and biofilm growth. Future work will evaluate AFE performance under large-scale field conditions in Yellow-River-irrigated farmlands.

5. Conclusions

In this study, a novel auto-flushing emitter (AFE) was developed, whose operating mode can be switched between normal irrigation and auto-flushing modes by adjusting H_0. Three cores (EMI1, EMI2, and EMI3) combined with three elastomers (SI, PU, and PTFE) were tested, including six AFEs and three CKs. The main findings are summarized as follows:

(1) Under clean water, q_{CW} of the AFEs increased stepwise with rising H_0, and H_j ranged from 0.07 to 0.10 MPa. In the auto-flushing mode, q_{CW} of SI-fitted AFEs was 1.96–17.88% higher than that of PU-fitted AFEs, while the PTFE-fitted CKs exhibited no stepped flow increase with H_0.

(2) Under sediment-laden water, *Dra* of all nine emitters gradually decreased with *T*. The reduction rate of *Dra* was suppressed at higher H_0 and for softer elastomers. Core type, elastomer material and H_0 all exerted significant effects on ΔDra ($P < 0.05$). At 360 min, *Dra* of SI-fitted AFEs exceeded that of the PU-fitted AFEs by 14.2% and the CKs by 30.2%.

(3) Correlation and regression analyses indicated that the enlarged *S* under auto-flushing mode is the primary factor responsible for the enhanced anti-clogging capacity. A larger *S*

facilitates sediment transport and discharge when $H_0 > H_j$. The v of SI-fitted AFEs overlapped the main range of U_c, providing favorable hydraulic conditions for sediment removal.

(4) Among all tested combinations, EMI2-SI and EMI3-SI are recommended for drip irrigation systems using sediment-laden water (2 g/L, d_{50}=34.84 μm). At H_0 = 0.08 MPa (normal irrigation mode), their q_{CW} were 0.71 and 0.98 L/h, with x of 0.452 and 0.497, respectively; at H_0 = 0.10 MPa (auto-flushing mode), their *Dra* remained above 75% throughout the 540 min test.

Laboratory results demonstrate that periodic pressure elevation can activate the auto-flushing function and mitigate emitter clogging. Field-scale tests under representative Yellow-River-irrigated agricultural conditions are required prior to large-scale practical promotion.

Statements and Declarations

Author contributions Q. Du and Z. Yang designed and performed the experiments, and collected long-term operational data. B. Yao and S. Sun provided experimental materials and experimental-condition support. H. Gao designed and prepared the figures and tables. Q. Du, Y. Zhang and H. Li carried out clogging-characteristic analysis, hydraulic calculation and data processing. Q. Du and Y. Mo established the overall research framework, interpreted the experimental results, and drafted the main manuscript text. Y. Mo oversaw the whole study, provided methodological guidance, and revised the manuscript. All authors have read, reviewed, and approved the final version of the manuscript.

Funding This research was funded by the Joint Fund for Yellow River Water Science Research of the National Natural Science Foundation of China (U2443211) and the Research

and Development Support Program of China Institute of Water Resources and Hydropower Research (ID0145C132026).

Data availability The datasets generated and analyzed during the current study are available from the corresponding author upon reason able request.

Declarations

Conflict of interest The authors declare no competing interests.

References

Aminpour Y, Amiri P, Maroufpoor E, Kamangar BB, Puig-Bargués J (2022) Effect of type of emitter self-cleaning mechanism and its structure on the performance of drip irrigation system using effluent of rainbow trout fish. Irrig Sci 40:163–175. https://doi.org/10.1007/s00271-022-00767-1

Archibong-Eso A, Aliyu AM, Yan W, Okeke NE, Baba YD, Fajemidupe O, Yeung H (2020) Experimental study on sand transport characteristics in horizontal and inclined two-phase solid-liquid pipe flow. J Pipeline Syst Eng Pract 11:04019050. https://doi.org/10.1061/(ASCE)PS.1949-1204.0000427

British Standards Institution (1992) BS 7605-2:1992. Agricultural irrigation equipment — emitters and emitting pipe — specification and test methods.

Chen X, Wu P, Fan X, Niu W (2008) Numerical simulation of structural parameters using CFD and anti-clogging design analyse on drip emitter. J Irrig Drain (2):35–38 (in Chinese). https://doi.org/10.13522/j.cnki.ggps.2008.02.012

Cheng Y, Xia J, Fang H, Zhou M, Zhou Z, Lu J, Li D, Falconer RA, Bai Y (2025) Modelling of flood risks to people's life and property in the lower Yellow River under different

489 floodplain management modes. Engineering 51:240–253.
490 https://doi.org/10.1016/j.eng.2025.02.011
491 Dallagi H, Ait Mouheb N, Soric A, Boiron O (2024) Simulation of the flow characteristics of
492 a labyrinth milli-channel used in drip irrigation. Biosyst Eng 239:114–129.
493 https://doi.org/10.1016/j.biosystemseng.2024.02.004
494 Dey S, Papanicolaou A (2008) Sediment threshold under stream flow: a state-of-the-art review.
495 KSCE J Civ Eng 12:45–60. https://doi.org/10.1007/s12205-008-8045-3
496 Frey B, Ehret DL, Bryla DR, Forge T, Helmer T (2012) Effects of drip irrigation
497 configuration and rate on yield and fruit quality of young highbush blueberry plants.
498 HortScience 47:414–421. https://doi.org/10.21273/HORTSCI.47.3.414
499 Gao H, Mo Y, Li Z, Li W, Zhang Y, Li H (2025) Regulation mechanism of automatic flushing
500 valve on emitter clogging characteristics during drip irrigation with Yellow River water.
501 J Hydraul Eng 56:1517–1528 (in Chinese).
502 https://doi.org/10.13243/j.cnki.slxb.20250281
503 Gao N (2023) Structural design and numerical simulation of a variable flow emitter for
504 subsurface drip irrigation. MSc thesis, Tianjin Agricultural University, Tianjin, China. (in
505 Chinese)
506 Gong X, Tao R, Hao Y, Zhang M, Yu G (2021) Critical velocity of sand transportation along
507 long straight pipeline. Port Waterw Eng (8):13–17, 23 (in Chinese).
508 https://doi.org/10.16233/j.cnki.issn1002-4972.20210728.014
509 Han S, Li Y, Xu F, Sun D, Feng J, Liu Z, Wang Z (2018) Effect of lateral flushing on emitter
510 clogging under drip irrigation with Yellow River water and a suitable method. Irrig Drain

67:199–209. https://doi.org/10.1002/ird.2193

Hou L, Zhang H, Li L, Li X (2024) Study on calculation of flow resistance and riverbed slope of the Yellow River. J Hydraul Eng 55:1020–1032 (in Chinese). https://doi.org/10.13243/j.cnki.slxb.20230752

Hu S, Li W, Yang G, Liu N (2020) Operation effect of improved straight-line desilting basin in agricultural micro-irrigation. J Drain Irrig Mach Eng 38:626–631. (in Chinese)

Kang S (2021) Accelerating the modernization of irrigation districts and the application of water-saving technologies to promote ecological protection and high-quality development in the Yellow River Basin. China Water Resour 17:4–7. (in Chinese)

Li D, Li Y, Wang Z, Wang X, Li Y (2016) Quantitative, SEM-based shape analysis of sediment particles in the Yellow River. Int J Sediment Res 31:341–350. https://doi.org/10.1016/j.ijsrc.2016.05.006

Li GY, Wang JD, Alam M, Zhao YF (2006) Influence of geometrical parameters of labyrinth flow path of drip emitters on hydraulic and anti-clogging performance. Trans ASABE 49:637–643. https://doi.org/10.13031/2013.20483

Li L, Zhang G, Wang Y (2018) Threshold probability and incipient motion velocity of uniform sediment on arbitrary slopes. J Sediment Res 43:38–43 (in Chinese). https://doi.org/10.16239/j.cnki.0468-155x.2018.03.007

Li Z, Mo Y, Wu F, Gao H, Wang R, Wang J (2025) The effects of an automatic flushing valve on the hydraulic performance of a subsurface drip irrigation system for alfalfa. Agriculture 15:1107. https://doi.org/10.3390/agriculture15101107

Liu Y, Li D, Wu P, Zhang L, Zhu D, Chen J (2018) Clogging characteristic of different

emitters in drip irrigation with hard water. Trans Chin Soc Agric Eng 34:96–102. (in Chinese)

Ma C, Jiang C, Li Y, Shi N, Liu S, Hu X, Liu Z, Sun Z, Muhammad T (2024) Effect of lateral flushing on emitter clogging in drip irrigation using high-sediment water. Agric Water Manag 293:108702. https://doi.org/10.1016/j.agwat.2024.108702

Mo Y, Zhao X, Wang J, Zhang Y, Gong S, Xia H, Li Q, Wang Y (2022) Design and structural optimization of the automatic flushing valve with exhaust function. Trans Chin Soc Agric Eng 38:72–79. (in Chinese)

Mo Y, Zhang Y, Wang D, Wang J, Li G, Gong S, Gao X (2024) Germination and growth of corn submitted to sowing and cultivation management by subsurface drip irrigation in the North China Plain. Irrig Sci 42:801–813. https://doi.org/10.1007/s00271-023-00900-8

Mo Y, Wang D, Gao N, Wang J, Zhang Y, Gong S, Gao X (2025) Drip irrigation variable emitter and testing system. CN Patent CN114402967B.

Niu P (2024) Structural optimization and numerical simulation study of variable flow emitters for subsurface drip irrigation with anti-sediment clogging features. MSc thesis, Tarim University, Alar, China. (in Chinese)

Niu W, Liu L, Chen X (2013) Influence of fine particle size and concentration on the clogging of labyrinth emitters. Irrig Sci 31:545–555. https://doi.org/10.1007/s00271-012-0328-2

Niu X, Mo Y, Gao H, Li Z, Hu Y, Gao X, Zhang Y, Zhang Q, Xiao X (2026) Predictive modelling and analysis of filtration performance for drip irrigation filters using sediment-laden water based on the differential evolution optimized random forest

(DE/RFR). Agriculture 16:844. https://doi.org/10.3390/agriculture16080844

Qian N, Wan Z (2003) Mechanics of sediment transport. Science Press, Beijing. (in Chinese)

Ren X, Liu Y, Zhang Z, Yao F, Jiang Y (2024) Standardizing the irrigation water sources for emitter anti-clogging test. Trans Chin Soc Agric Eng 40:79–88. (in Chinese)

Shen Y, Puig-Bargués J, Li M, Xiao Y, Li Q, Li Y (2022) Physical, chemical and biological emitter clogging behaviors in drip irrigation systems using high-sediment loaded water. Agric Water Manag 270:107738. https://doi.org/10.1016/j.agwat.2022.107738

Shen Y, Liu J, Xiao Y, Yang S (2026) Mechanism of sediment particle incipient motion governed by turbulent structures in open channel flows. Adv Water Sci 37:563–573 (in Chinese). https://doi.org/10.14042/j.cnki.32.1309.2026.03.014

Standardization Administration of China (SAC) (2009) GB/T 17187-2009. Agricultural irrigation equipment — emitters and emitting pipe — specification and test methods.

Sun L, Jin Z, Sun Z, Shen G, Zheng H, Guo C, Li L (2025) Critical criteria for sediment suspension derived from suspension probability. Eng Sci Technol Int J 64:102034. https://doi.org/10.1016/j.jestch.2025.102034

Tang H, Yuan S, Cao H (2023) Theory and practice of hydrodynamic reconstruction in plain river networks. Engineering 24:202–211. https://doi.org/10.1016/j.eng.2022.01.015

Tang X, Zhao X, Li Y, Li X (2018) Numerical simulation of flow fields and particle movement characteristics in labyrinth channel emitter using different turbulence models. Trans Chin Soc Agric Eng 34:120–128. (in Chinese)

Wang L (2022) Mechanical properties of materials. Chemical Industry Press, Beijing. (in Chinese)

Wang M, Xue M, Sun H, Li H, Li R, Han Q (2025) Investigating sedimentation patterns and fluid movement in drip irrigation emitters in the Yellow River Basin. Water 17:910. https://doi.org/10.3390/w17070910

Wang Y, Zhu D, Zhang L, Niu W, Zhang Z, Ren G (2014) Experiment on sediment distribution in lateral pipes and clogging of emitter. Trans Chin Soc Agric Mach 45:177–182. (in Chinese)

Xiang Y (2024) Mechanism and control methods of blockage in drip irrigation emitters from the Yellow River. MSc thesis, Gansu Agricultural University, Lanzhou, China. (in Chinese)

Xing S, Du K, Liu N, Li M, Wen Y, Juana L, Sánchez R, Zhang J, Wang Z (2025) Evaluation of the effects of dynamic pressure and emitter type on clogging in drip irrigation systems. Agric Water Manag 321:109916. https://doi.org/10.1016/j.agwat.2025.109916

Xu T, Bao S, Li Z, Yu Q, Zheng E (2023) The study of structural optimization on hydraulic performance and anti-clogging performance of labyrinth drip irrigation emitters. Agronomy 13:2496. https://doi.org/10.3390/agronomy13102496

Xu X (2025) The Yellow River Basin should promote the coordinated construction of supporting facilities in Yellow River diversion irrigation districts. Consult Forum 4:44. (in Chinese)

Yang B, Wu Y, Wang J, Ma X, Wang H, Zhang Y, Mo Y (2019) Anti-clogging performance analysis and structure optimization simulation for dental labyrinth emitter. J Irrig Drain 38:84–89, 128 (in Chinese). https://doi.org/10.13522/j.cnki.ggps.20190174

Yang B, Wang J, Zhang Y, Wang H, Ma X, Mo Y (2020) Anti-clogging performance

599 optimization for dentiform labyrinth emitters. Irrig Sci 38:1–11.
600 https://doi.org/10.1007/s00271-020-00671-6
601 Yang Z, Mo Y, Zhao C, Liu H, Zhang Y, Xiao J, Gong S, Bi Y (2024) Multi-objective
602 optimization design of the small flow rate emitter structure based on the NSGA-II
603 genetic algorithm. Agriculture 14:2336. https://doi.org/10.3390/agriculture14122336
604 Yang Z (2025) Numerical simulation and multi-objective structural optimization of a
605 small-flow self-cleaning variable emitter. MSc thesis, Taiyuan University of Technology,
606 Taiyuan, China. (in Chinese)
607 Yu L, Li N, Liu X, Yang Q, Li Z, Long J (2019) Influence of dentation angle of labyrinth
608 channel of drip emitters on hydraulic and anti-clogging performance. Irrig Drain 68:256–
609 267. https://doi.org/10.1002/ird.2304
610 Yuan J, Zhu D, Sun S, Zheng C, Nazarov K, Liu C (2024) Optimization of structural
611 parameter for disc filter in drip irrigation system. Trans Chin Soc Agric Eng 40:133–141.
612 (in Chinese)
613 Zha Y, Hou P, Liu Z, Zhang K, Xiao Y, Li Y (2023) Effect of inclined-tube on the removal
614 performance of fine sediment in a gravity sedimentation tank. J Irrig Drain 42:127–135.
615 https://doi.org/10.1002/ird.70046
616 Zhang L, Li S (2017) Numerical experimental investigation of douche hydraulic performance
617 on drop irrigation of tooth-type labyrinth channel. Water Resour Power 35:103–106 (in
618 Chinese). https://doi.org/10.20040/j.cnki.1000-7709.2017.08.026
619 Zhang W, Lv C, Zhao X, Dong A, Niu W (2021) The influence mechanism of the main
620 suspended particles of Yellow River sand on the emitter clogging — an attempt to

improve the irrigation water utilization efficiency in Yellow River basin. Agric Water Manag 258:107202. https://doi.org/10.1016/j.agwat.2021.107202

Zhu X, Yu L, Li N, Wang D (2025) Investigation of clogging mechanism and hydrodynamic behavior of sediment movement in patch-type drip irrigation emitters. J Drain Irrig Mach Eng 43:749–756.